Electronic Supplementary Material (ESI) for Physical Chemistry Chemical Physics.

Effects of temperature and pressure on the optical and vibrational properties of thermoelectric SnSe

Ilias Efthimiopoulos,[1,*] Matthias Berg,[2,†] Annika Bande,[2] Ljiljana Puskar,[2] Eglof Ritter,[3] Wei Xu,[4] Augusto Marcelli,[5,6] Michele Ortolani,[7] Martin Harms,[1] Jan Müller,[1] Sergio Speziale,[1] Monika Koch-Müller,[1] Yong Liu,[8] Li-Dong Zhao,[9] and Ulrich Schade[2]

[1] *GFZ German Research Centre for Geosciences, Telegrafenberg, 14473 Potsdam, Germany*
[2] *Institute of Methods for Material Development, Helmholtz-Zentrum Berlin für Materialien und Energie, Albert-Einstein-Strasse 15, 12489 Berlin, Germany*
[3] *Institute of Biology, Humboldt-Universität zu Berlin, Invalidenstrasse 42, 10115 Berlin, Germany*
[4] *Beijing Synchrotron Radiation Facility, Institute of High Energy Physics, Chinese Academy of Sciences, 100049 Beijing, PR China*
[5] *INFN-Laboratori Nazionali di Frascati, Via E. Fermi 40, Frascati, 00044, Italy*
[6] *RICMASS, Rome International Center for Materials Science Superstripes, Via dei Sabelli 119A, 00185 Rome, Italy*
[7] *Department of Physics, University of Rome La Sapienza, P.le A. Moro 2, 00185 Rome, Italy*
[8] *AECC-Beijing Institute of Aeronautical Materials, No. 8 Hangcai Avenue, Huanshancun, Haidian District, 100095 Beijing, PR China*
[9] *School of Materials Science and Engineering, No. 37 Xueyuan Road, Haidian District, Beihang University, 100191 Beijing, PR China*

(Dated: February 8, 2019)

---

[*] iliefthi@gfz-potsdam.de
[†] matthias.berg@helmholtz-berlin.de

I. SUPPLEMENTARY MATERIAL

A. High-temperature FIR reflectance spectra of SnSe

The normal incidence reflectance R of a material at frequency ω is given by the relationship [1]:

$$R(\omega) = \left| \frac{\sqrt{\varepsilon(\omega)} - 1}{\sqrt{\varepsilon(\omega)} + 1} \right| \tag{1}$$

where $\varepsilon(\omega)$ is the complex dielectric function of the compound. In our case, the SnSe reflectance spectra for the *b*- and *c*-axis have been fitted with the Drude-Lorentz model, where $\varepsilon(\omega)$ can be approximated by a sum of j transverse optical (TO) oscillators/ phonons:

$$\varepsilon(\omega) = \varepsilon_1(\omega) + i\varepsilon_2(\omega) = \varepsilon_\infty + \sum_j \frac{\omega_j^2}{f_j^2 - \omega^2 - i\omega\Gamma_j} \tag{2}$$

with ε_∞ the (electronic) high-frequency dielectric constant for ω much larger than the respective FIR frequencies, and f_j, ω_j, and Γ_j the oscillator strength, the TO oscillator frequency, and the damping constant of the respective TO oscillator, respectively. The real $\varepsilon_1(\omega)$ and imaginary $\varepsilon_2(\omega)$ parts are consequently equal to [1]:

$$\begin{aligned} \varepsilon_1(\omega) &= \varepsilon_\infty + \sum_j f_j \omega_j^2 \frac{\omega_j^2 - \omega^2}{(\omega_j^2 - \omega^2)^2 + \omega^2\Gamma_j^2} \\ \varepsilon_2(\omega) &= \sum_j f_j \omega_j^2 \frac{\Gamma_j \omega}{(\omega_j^2 - \omega^2)^2 + \omega^2\Gamma_j^2} \end{aligned} \tag{3}$$

Moreover, the respective longitudinal optical (LO) phonon frequencies can be estimated from the maxima of the ε_1 or, equivalently, from the maxima of the energy loss function, which is defined as the imaginary part of -$\frac{1}{\varepsilon(\omega)}$:

$$Im\left(-\frac{1}{\varepsilon(\omega)}\right) = \frac{\varepsilon_2(\omega)}{\varepsilon_1^2(\omega) + \varepsilon_2^2(\omega)} \tag{4}$$

The fitting of the SnSe reflectance spectra at ambient temperature (RT) for both *b*- and *c*-crystal orientations is shown in Fig. 1, and the extracted oscillator and ε_∞ parameters, alongside our DFT-PBEsol0 and literature results [2, 3] are listed in Table I, where we can observe a very good agreement between various sources.

Upon increasing temperature, however, fitting of the measured reflectance spectra became quite challenging. For example, the TO-phonon smears out and a Drude-like contribution emerges at low frequencies in the 795 K spectrum along the *b*-axis. By ignoring the data above 250 cm^{-1} and the dip at 173 cm^{-1} (the latter feature looks unchanged for all temperatures, Fig. 2 in the main text), we fit the spectrum with two oscillators at 58 cm^{-1} and 84 cm^{-1}. The total spectral weight is almost conserved with T, and the refractive index was kept at the RT value. The first oscillator at 58 cm^{-1} may represent free-carrier spectral weight, whereas the second TO phonon at 84 cm^{-1} is downshifted from its RT frequency value of 94 cm^{-1} and smeared out considerably (Γ increased from 7 cm^{-1} to 63 cm^{-1}). All these modifications can be attributed to the TO-phonon screening by the T-induced enhancement of the free carrier concentration in SnSe at these temperatures.

In the next (and highest-T) *b*-axis reflectance spectrum collected at 845 K, the Drude-like contribution was kept unchanged for fitting purposes. In order to fit the Lorentz model at this temperature, a new phonon had to be added at 140 cm^{-1}. The aforementioned TO mode at 84 cm^{-1} is still present, but with diminished intensity and spectral weight compared to the previous 795 K spectrum. Part of this 'lost' spectral weight transfers into the new 140 cm^{-1} phonon. Given that the adoption of the *Bbmm* phase is expected above ∼800 K [4–7], the 'appearance' of this new 140 cm^{-1} mode might constitute the FIR fingerprint of the T-induced *Pnma* → *Bbmm* structural transition. The significant free carrier screening of both TO phonons, however, does not allow for a more quantitative discussion and reaching definite conclusions at this stage.

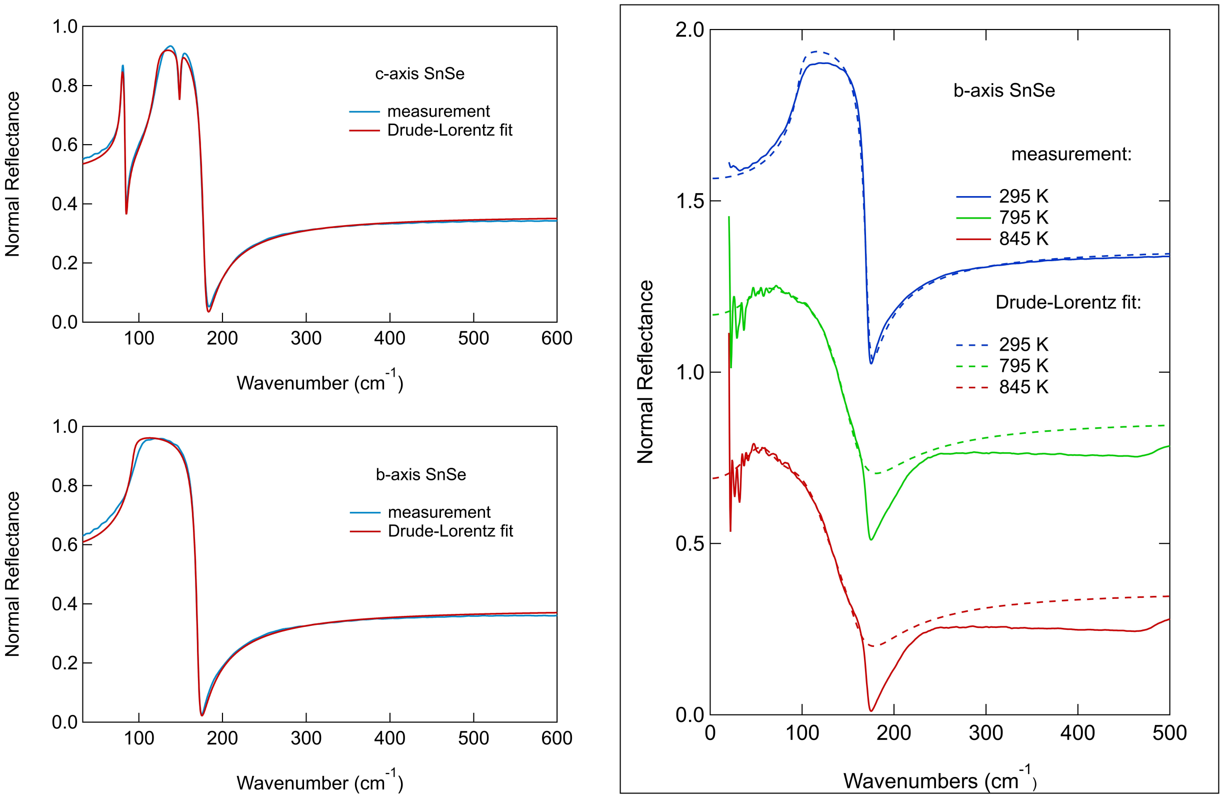

FIG. 1: (a) Measured FIR reflectance spectra (blue color), alongside the corresponding Drude-Lorentz fits (red color) for the c- and b-axis of SnSe at ambient conditions. (b) Measured FIR reflectance spectra (solid lines), alongside the corresponding Drude-Lorentz fits (dashed lines) for the b-axis of SnSe at 295 K (RT, blue), at 795 K (green), and at 845 K (red).

TABLE I: Optical parameters for the SnSe $Pnma$ phase at ambient conditions, as derived from the Drude-Lorentz fit of the experimental reflectance spectra (Fig. 1). The values are compared with published data (Ref. 2: †, Ref. 3: ⋄) and to our DFT-PBEsol0 calculations (in bold).

Optical parameters	$\overrightarrow{E}//\overrightarrow{a}$	$\overrightarrow{E}//\overrightarrow{b}$	$\overrightarrow{E}//\overrightarrow{c}$
ω_{TO1} (cm^{-1})	$(56\pm5^{\dagger}, 48^{\diamond})$; **55**	-	79 ± 2 $(80\pm5^{\dagger})$; **92**
f_{TO1}	**0.4**	-	6.1 ± 6; **6**
Γ_{TO1} (cm^{-1})	-	-	2.1 ± 5
ω_{LO1} (cm^{-1})	$(57\pm5^{\dagger}, 60^{\diamond})$; **55**	-	84 ± 4 $(85\pm5^{\dagger})$; **96**
ω_{TO2} (cm^{-1})	$(130\pm5^{\dagger}, 124^{\diamond})$; **135**	-	121 ± 3 $(123\pm5^{\dagger})$; **128**
f_{TO2}	**19**	-	16.7 ± 7; **18**
Γ_{TO2} (cm^{-1})	-	-	6.7 ± 8
ω_{LO2} (cm^{-1})	$(141\pm5^{\dagger}, 155^{\diamond})$; **206**	-	148 ± 4 $(149\pm5^{\dagger})$; **202**
ω_{TO3} (cm^{-1})	$(142\pm10^{\dagger}, 152^{\diamond})$; **150**	94 ± 2 $(96\pm5^{\dagger})$; **94**	149 ± 3 $(150\pm5^{\dagger})$; **159**
f_{TO3}	**0.02**	42 ± 2 ; **58**	0.17 ± 5; **0.3**
Γ_{TO3} (cm^{-1})	-	4.9 ± 5	2.5 ± 5
ω_{LO3} (cm^{-1})	$(191\pm10^{\dagger}, 181^{\diamond})$; **150**	171 ± 2 $(172\pm5^{\dagger})$; **192**	179 ± 3 $(180\pm5^{\dagger})$; **159**
ω_{TO4} (cm^{-1})	$(75^{\diamond})$	-	-
f_{TO4}	-	-	-
Γ_{TO4} (cm^{-1})	-	-	-
ω_{LO4} (cm^{-1})	$(85^{\diamond})$	-	-
ε_{∞}	$(16\pm2^{\dagger}, 16^{\diamond})$; **14.4**	18 ± 1 $(17\pm2^{\dagger})$; **18.2**	16 ± 2 $(13\pm2^{\dagger})$; **14.3**

B. Basis Sets

Basis sets are reported in CRYSTAL format [8].

The all-electron 9-7631-511*d* Gaussian basis set for Se, optimized for SnSe, is based on the atomic version by Towler [9]. The most diffuse *sp*-function was deleted and an additional diffuse *d*-function was added.

```
34 8
0 0 9 2.0 1.0
 2275090.0 0.000038
 319959.0 0.0003344
 64974.1 0.0021238
 15718.0 0.011193
 4347.15 0.047900
 1367.7 0.157400
 483.334 0.352332
 187.066 0.423303
 75.1333 0.153645
0 1 7 8.0 1.0
 5241.62 −0.000373 0.0009764
 1192.97 −0.0072305 0.0092853
 354.263 −0.061887 0.056735
 121.56 −0.145788 0.218068
 46.765 0.246071 0.447931
 19.7469 0.712463 0.395229
 8.44148 0.239375 0.09678
0 1 6 8.0 1.0
 103.375 0.0039064 −0.014826
 36.4438 −0.054067 −0.071387
 15.4097 −0.323251 0.116639
 6.326 0.264172 0.970063
 2.62943 0.954686 1.21262
 1.04921 0.236846 0.328426
0 3 5 10.0 1.0
 202.635 0.005270
 59.7021 0.04036
 21.5166 0.162038
 8.3345 0.368724
 3.15228 0.46438
0 3 1 0.0 1.0
 1.11207870156 1.0
0 3 1 0. 1.
 0.305992425616 1.
0 1 3 6.0 1.0
 2.318094 −0.908900 −0.1759
 0.945900 −0.595800 0.5555
 0.409815 3.163300 2.8121
0 1 1 0.0 1.0
 0.129408101621 1.0 1.0
```

ECP28MDF-411-51*d* for Sn, optimized for SnSe, based on the solid state version by Baranek [10], which in turn is based on the atomic/molecular version by Metz *et al.* [11].

```
22. 0 2 4 4 2 0
 17.420414 279.988682 0
 7.631155 62.377810 0
 16.131024 66.162523 0
 15.628077 132.174396 0
 7.325608 16.339417 0
 6.942519 32.488959 0
 15.514976 36.387441 0
 15.188160 54.507841 0
 5.456024 8.696823 0
 5.363105 12.840208 0
 12.282348 −12.576333 0
 12.272150 −16.595944 0
0 1 4 8. 1.
 12.0606722098 0.0844070512669 0.0368811742301
 8.03066973225 −0.185102525393 −0.234782434687
```

```
 2.45748084227 0.0837343892348 0.621356592737
 1.01390396118 0.619389030077 0.015620738282
0 1 1 4. 1.
 0.976163308883 1. 1.
0 1 1 0. 1.
 0.170467605149 1. 1.
0 3 5 10. 1.
 10.6273770193 −0.0108186550584
 4.91418243094 0.112610228075
 2.48328701349 0.426680918513
 1.15089341028 0.376555012814
 0.698258653292 0.232892476577
0 3 1 0. 1.
 0.301796007677 1.
```

C. Structural changes in SnSe under pressure

The measured XRD diffractograms of SnSe at various pressures are presented collectively in Fig. 2. We can readily observe that the starting *Pnma* phase is stable up to 10.3 GPa, with the obtained patterns allowing for full Rietveld refinements [Fig. 4 in the main text]. Above that pressure, the *Pnma* structural model can no longer reproduce the XRD patterns. Consequently, we indexed the XRD diffractograms with the proposed *Bbmm* phase above that pressure (Fig. 2) [12]. Unfortunately, the measured XRD patterns suffered from severe contamination from the argon PTM and the rhenium gasket Bragg peaks [marked as exclamation marks and asterisks in Fig. 2, respectively], hindering in turn the unambiguous assignment to the *Bbmm* phase. For this purpose, we performed a second high-pressure XRD experiment, where we raised pressure directly to ∼21 GPa and allowed for sufficient relaxation time. In this second attempt, we managed to index the SnSe high-pressure phase to the SG *Bbmm* (Fig. 4 in the main text). Finally, we should mention the very good agreement between the experimentally determined and calculated Sn and Se atomic coordinates (Fig. 2), which in turn compare consistently with earlier XRD results [12].

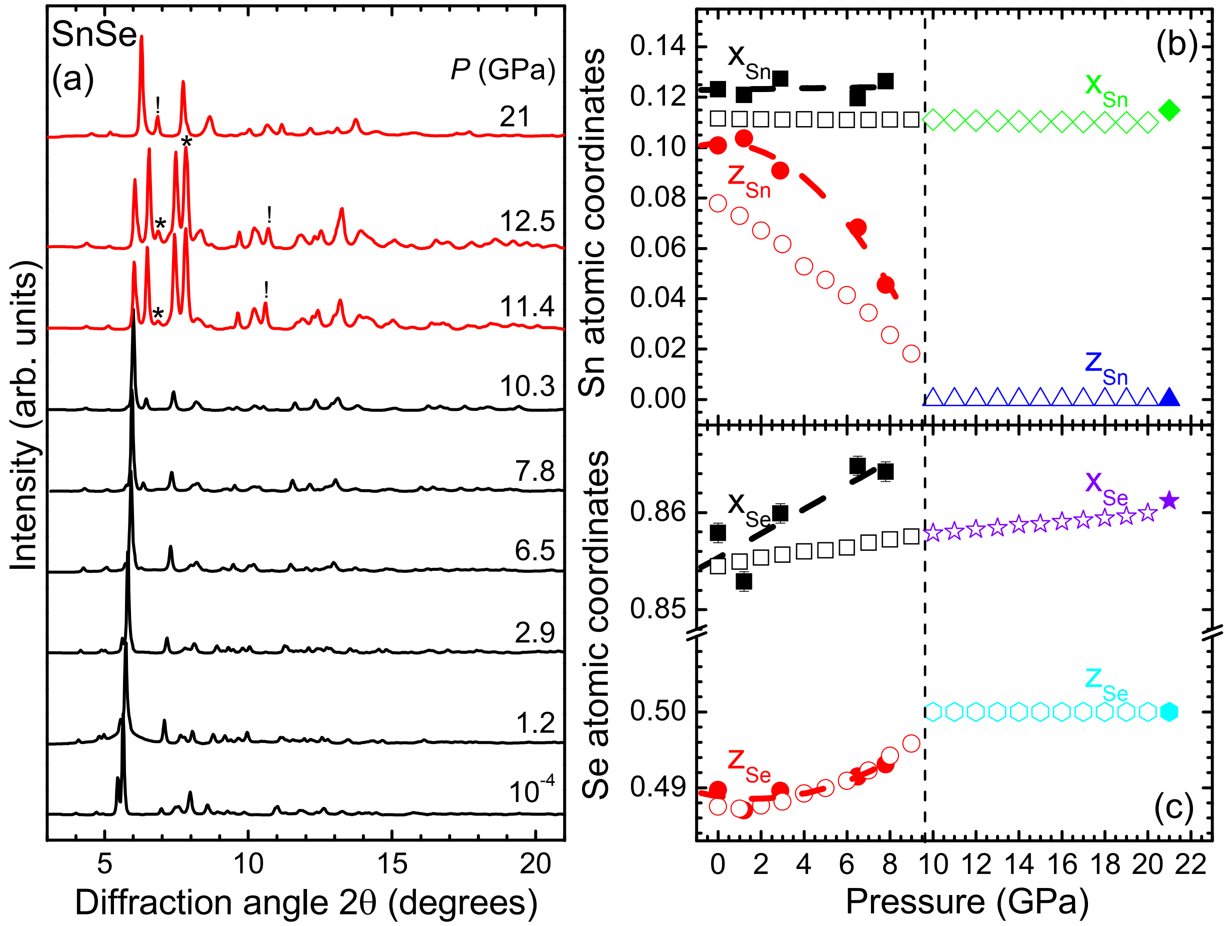

FIG. 2: (a) Selected XRD patterns of SnSe at various pressures (T = 300 K, λ = 0.29 Å). The ambient-pressure *Pnma* and the high-pressure *Bbmm* modifications are shown in black and red, respectively. Asterisks and exclamation marks indicate the strongest rhenium (gasket material) and argon (PTM) Bragg peaks. (b) Sn and (c) Se atomic coordinates as a function of pressure. The dashed lines serve as guides for the eye (experimental data: solid symbols, calculated DFT-PBEsol0 data: open symbols). The vertical dashed line marks the onset of the *Pnma* → *Bbmm* structural transition. Error bars lie within the symbols.

TABLE II: Results of the DFT-PBEsol0 structural optimizations of SnSe under external hydrostatic pressures for space group *Pnma*. The respective lattice constants of the conventional unit cell and the Sn and Se fractional coordinates (x_{Sn}, z_{Sn}; x_{Se} and z_{Se}) are listed (y_{Sn} = y_{Se} = 0.25).

P (GPa)	a (Å)	b (Å)	c (Å)	V (Å^3)	x_{Sn}	z_{Sn}	x_{Se}	z_{Se}
0.0	11.306	4.146	4.324	202.69	0.11148	0.07783	0.85447	0.48752
1.0	11.247	4.131	4.285	199.09	0.11128	0.07287	0.85495	0.48724
2.0	11.193	4.118	4.247	195.76	0.11118	0.06709	0.85535	0.48767
3.0	11.144	4.106	4.214	192.82	0.11107	0.06168	0.85567	0.48815
4.0	11.104	4.095	4.176	189.89	0.11119	0.05287	0.85602	0.48921
5.0	11.060	4.082	4.149	187.31	0.11101	0.04743	0.85611	0.48993
6.0	11.019	4.070	4.124	184.95	0.11098	0.04143	0.85641	0.49090
7.0	10.972	4.057	4.103	182.64	0.11101	0.03449	0.85689	0.49227
8.0	10.933	4.046	4.082	180.57	0.11106	0.02562	0.85722	0.49422
9.0	10.893	4.034	4.065	178.63	0.11104	0.01816	0.85755	0.49584
10.0	10.853	4.024	4.049	176.83	0.11108	0.00084	0.85793	0.49984
11.0	10.818	4.009	4.038	175.13	0.11085	0.00002	0.85803	0.49999
12.0	10.782	3.997	4.027	173.55	0.11068	0.00014	0.85826	0.49997
13.0	10.750	3.982	4.015	171.87	0.11054	0.00000	0.85844	0.50000
14.0	10.716	3.969	4.006	170.38	0.11047	0.00013	0.85873	0.49995
15.0	10.687	3.958	3.995	168.99	0.11029	0.00004	0.85883	0.49999
16.0	10.658	3.946	3.986	167.64	0.11022	0.00000	0.85903	0.50000
17.0	10.630	3.934	3.978	166.35	0.11013	0.00015	0.85922	0.49996
18.0	10.602	3.923	3.969	165.08	0.11003	0.00005	0.85940	0.49998
19.0	10.574	3.911	3.961	163.81	0.10997	0.00004	0.85959	0.49999
20.0	10.546	3.900	3.955	162.67	0.11002	0.00000	0.85993	0.50000

TABLE III: Results of the DFT-PBEsol0 structural optimizations of SnSe under external hydrostatic pressures for space group *Bbmm*. The respective lattice constants of the conventional unit cell and the Sn and Se fractional coordinates (x_{Sn} and x_{Se}) are listed (y_{Sn} = y_{Se} = 0.25, z_{Sn} = 0, z_{Se} = 0.5).

P (GPa)	a (Å)	b (Å)	c (Å)	V (Å^3)	x_{Sn}	x_{Se}
0.0	11.398	4.192	4.200	200.68	0.11466	0.85437
1.0	11.322	4.170	4.181	197.39	0.11404	0.85489
2.0	11.254	4.151	4.162	194.43	0.11354	0.85536
3.0	11.193	4.132	4.145	191.70	0.11301	0.85564
4.0	11.139	4.113	4.127	189.08	0.11245	0.85574
5.0	11.087	4.097	4.112	186.78	0.11208	0.85605
6.0	11.037	4.081	4.097	184.54	0.11178	0.85639
7.0	10.983	4.066	4.085	182.42	0.11156	0.85688
8.0	10.940	4.051	4.072	180.46	0.11138	0.85722
9.0	10.896	4.037	4.060	178.59	0.11117	0.85751
10.0	10.855	4.024	4.049	176.86	0.11104	0.85786
11.0	10.818	4.009	4.038	175.13	0.11085	0.85803
12.0	10.782	3.997	4.027	173.55	0.11068	0.85826
13.0	10.750	3.982	4.015	171.87	0.11054	0.85844
14.0	10.716	3.969	4.006	170.38	0.11047	0.85873
15.0	10.687	3.958	3.995	168.99	0.11029	0.85883
16.0	10.658	3.946	3.986	167.64	0.11022	0.85903
17.0	10.630	3.934	3.978	166.35	0.11012	0.85922
18.0	10.602	3.923	3.969	165.08	0.11003	0.85940
19.0	10.574	3.911	3.961	163.39	0.10997	0.85959
20.0	10.546	3.900	3.955	162.67	0.11002	0.85993

D. Complementary vibrational data of SnSe

In order to assign the IR- and Raman-active vibrations of the starting SnSe *Pnma* phase to specific atomic motions, we have calculated the corresponding phonon eigenvectors at ambient pressure. The obtained results are presented in Figs. 3-4. The structural input parameters are listed in Table II. Our results are in good agreement with previous

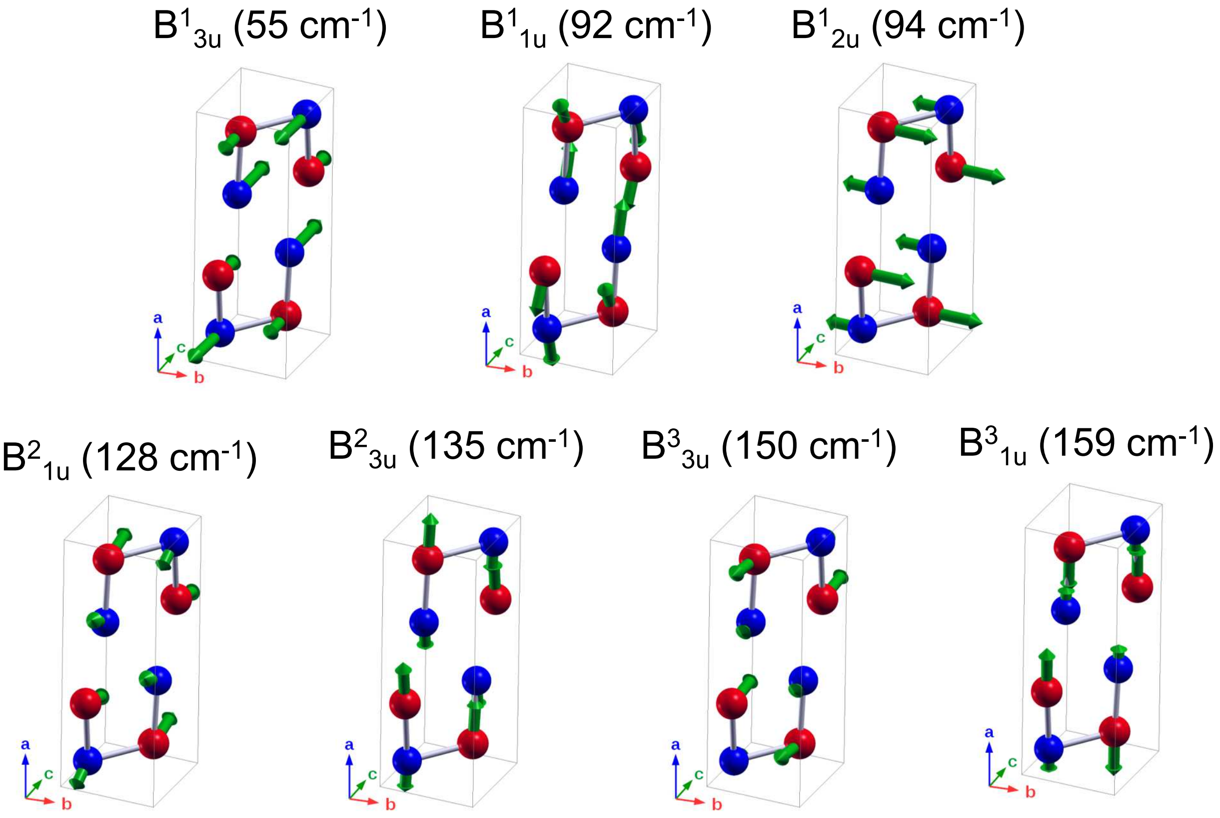

FIG. 3: Calculated eigenvectors for the IR-active modes of the *Pnma* SnSe phase at ambient pressure and zero temperature. The blue and red spheres correspond to Sn and Se atoms, respectively. The structural parameters used for the calculations are listed in Table II. The phonon eigenvectors have been visualized with the program XCrySDen [14].

Raman-active eigenvectors reported for the *Pnma*-SnSe phase [13].

Furthermore, in order to corroborate our high-pressure Raman results, we have additionally performed high-pressure far-infrared (FIR) absorbance measurements on SnSe powder (ground from single crystals) diluted in petroleum jelly; the latter acted also as a pressure transmitting medium (PTM), since it does not exhibit any IR activity, unlike the argon PTM used in our high-pressure XRD and Raman studies [15]. The experiments were conducted with the newly commissioned FIR microscope at the IRIS beamline, BESSY II synchrotron facility, coupled to a Vertex 70v Fourier-transform infrared spectrometer. The spectra were collected in the 50-600 cm^{-1} frequency region with a spectral resolution of 2 cm^{-1}, with a liquid helium-cooled bolometer as detector and a silicon beamsplitter. The microscope was continuously purged with nitrogen gas to avoid contamination of the spectra from the air atmosphere. The measured FIR spectra were averaged over 1024 scans. The ruby fluorescence method was employed for pressure calibration [16].

The results are shown in Fig. 5. At ambient conditions we can detect one broad IR feature close to $\sim$160 cm^{-1}, which can be assigned to B$_{1u}$ symmetry (B$^3_{1u}$ mode in Fig. 3). Increasing pressure shifts the B$_{1u}$ vibration to higher frequencies up to 8 GPa. Above this pressure, the pressure dependence of the frequency decreases sizeably by one order of magnitude (Table I in the main text), i.e. the mode becomes substantially less compressible. In addition, the intensity of this feature diminishes progressively with compression, and drops significantly after 8 GPa (Fig. 5). Taken together with our high-pressure XRD and Raman investigations, we attribute these FIR absorbance changes to the pressure-induced $Pnma \rightarrow Bbmm$ structural transition. We note that the smaller $Pnma \rightarrow Bbmm$ transition pressure value determined in the FIR experiment is most likely attributed to the less hydrostatic conditions imposed by the petroleum jelly PTM compared to the argon PTM used in the XRD and Raman studies [17]. Our DFT calculations have reproduced accurately the pressure-induced behavior of the B$^3_{1u}$ IR-active mode in terms of frequency and intensity compared to the experimental results (Fig. 5). Interestingly, the B$^3_{1u}$ FIR vibration is absent in the high-pressure *Bbmm* phase according to our DFT study (Table V), as this vibration shifts from the center Γ to the edge (Z-point) of the Brillouin zone upon the $Pnma \rightarrow Bbmm$ structural transition (not shown). Hence, the 'persistence' of the B$^3_{1u}$ mode after the $Pnma \rightarrow Bbmm$ transition in the experimental case could most likely be attributed to the non-hydrostatic conditions inside the sample chamber due to the presence of the petroleum jelly PTM, i.e. the

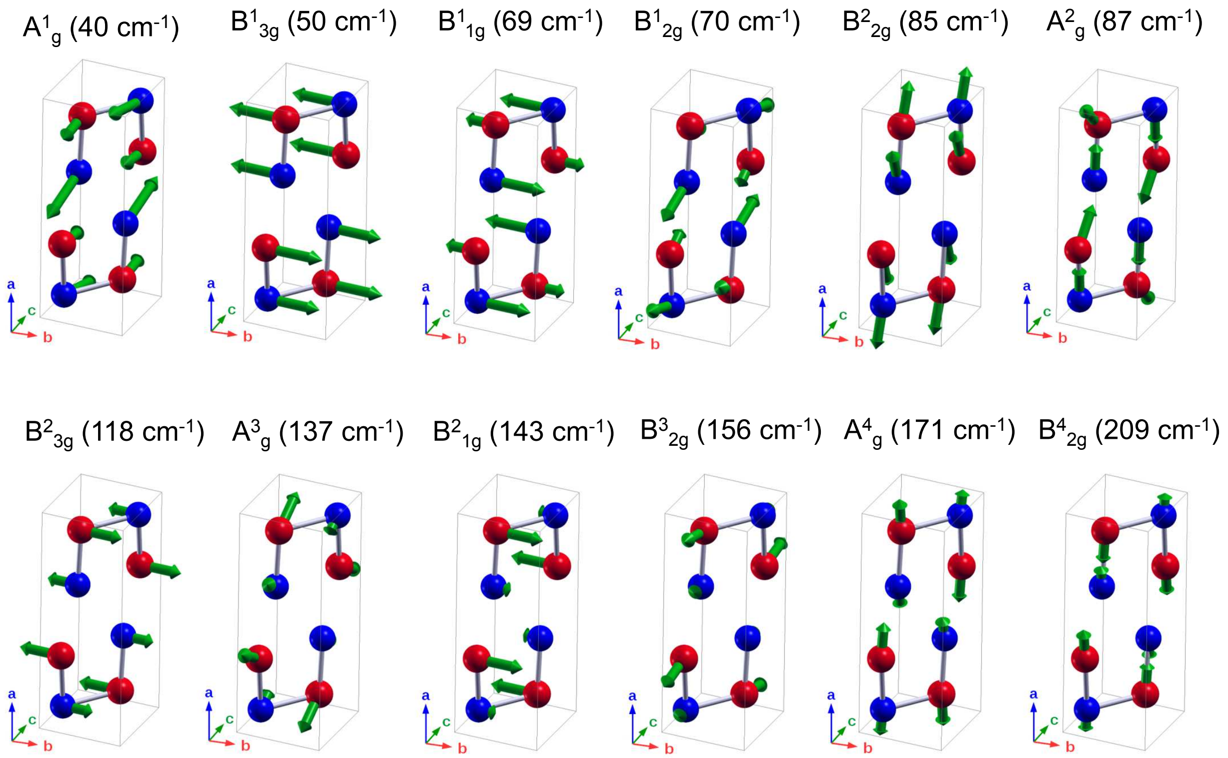

FIG. 4: Calculated eigenvectors for the Raman-active modes of the *Pnma* SnSe phase at ambient pressure and zero temperature. The blue and red spheres correspond to Sn and Se atoms, respectively. The structural parameters used for the calculations are listed in Table II. The phonon eigenvectors have been visualized with the program XCrySDen [14].

TABLE IV: Results of the DFT-PBEsol0 IR-active modes for the SnSe *Pnma* phase under external hydrostatic pressures. The respective mode assignments, mode frequencies ω_0, pressure dependence, and the isothermal γ_i^T mode Grüneisen parameters are provided. The latter have been calculated from the equation $\gamma_i^T = \frac{B_0}{\omega_0} \times \frac{\partial \omega}{\partial P}$, where we have used the calculated *Pnma* bulk modulus value $B_0 = 51.2$ GPa (Table II in the main text).

Mode assignment	ω_0 (cm^{-1})	$\frac{\partial \omega}{\partial P}$ (cm^{-1}/GPa)	γ_i^T
B$^1_{3u}$ ($\overrightarrow{E}//\overrightarrow{a}$)	54.54	-1.53	-1.44
B$^1_{1u}$ ($\overrightarrow{E}//\overrightarrow{c}$)	91.79	0.61	0.34
B$^1_{2u}$ ($\overrightarrow{E}//\overrightarrow{b}$)	93.56	-4.86	-2.66
B$^2_{1u}$ ($\overrightarrow{E}//\overrightarrow{c}$)	128.24	-2.49	-0.99
B$^2_{3u}$ ($\overrightarrow{E}//\overrightarrow{a}$)	135.24	1.92	0.73
B$^3_{3u}$ ($\overrightarrow{E}//\overrightarrow{a}$)	150.45	0.69	0.24
B$^3_{1u}$ ($\overrightarrow{E}//\overrightarrow{c}$)	159.32	2.94	0.95

pressure acting on the sample is not uniform (see e.g. Ref. 18 for relevant discussion). The calculated *Pnma* and *Bbmm* FIR-mode parameters at various pressures are tabulated in Table IV and Table V, respectively.

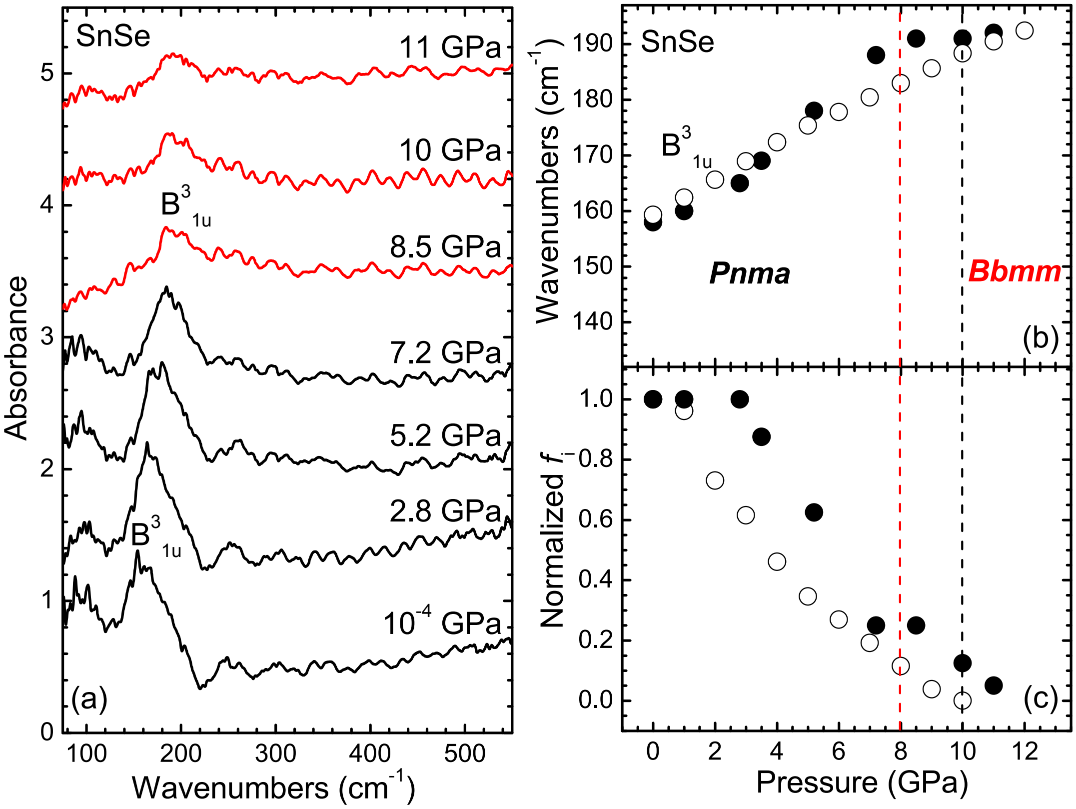

FIG. 5: (a) FIR absorbance spectra of SnSe at selected pressures. The black and red spectra correspond to the *Pnma* and the high-pressure *Bbmm* phases, respectively. The spectra have been shifted vertically for clarity. (b) Pressure-induced evolution of the *Pnma*-SnSe B^3_{1u} FIR mode frequency and (c) the respective normalized oscillator strength f_i at ambient temperature. The closed and open symbols correspond to experimental and DFT-PBEsol0 calculated data, respectively. The red and black vertical dashed lines represent the onset of the *Pnma* → *Bbmm* structural transition as determined in the FIR absorbance and the XRD studies, respectively.

TABLE V: Results of the DFT-PBEsol0 IR-active modes for the SnSe *Bbmm* phase under external hydrostatic pressures. The respective mode assignments, mode frequencies ω, pressure dependence, and the isothermal γ_i^T mode Grüneisen parameters are provided. The latter have been calculated from the equation $\gamma_i^T = \frac{B_0}{\omega_0} \times \frac{\partial\omega}{\partial P}$, where we have used the calculated *Bbmm* bulk modulus value $B = 95.2$ GPa (Table II in the main text). The IR mode frequencies ω are evaluated at the *Pnma* → *Bbmm* structural transition pressure of 10 GPa.

Mode assignment	ω (cm^{-1})	$\frac{\partial\omega}{\partial P}$ (cm^{-1}/GPa)	γ_i^T
B_{3u} ($\overrightarrow{E}//\overrightarrow{b}$)	49.02	2.26	4.39
B_{1u} ($\overrightarrow{E}//\overrightarrow{c}$)	107.44	3.37	2.99
B_{2u} ($\overrightarrow{E}//\overrightarrow{a}$)	154.09	1.22	0.75

Except from the IR-active modes, we have additionally calculated the respective Raman-active vibrations for both the SnSe *Pnma* and high-pressure *Bbmm* modifications. The results are listed in Tables VI-VII. The calculated (polycrystalline) Raman spectra of SnSe upon compression are also provided (Fig. 6).

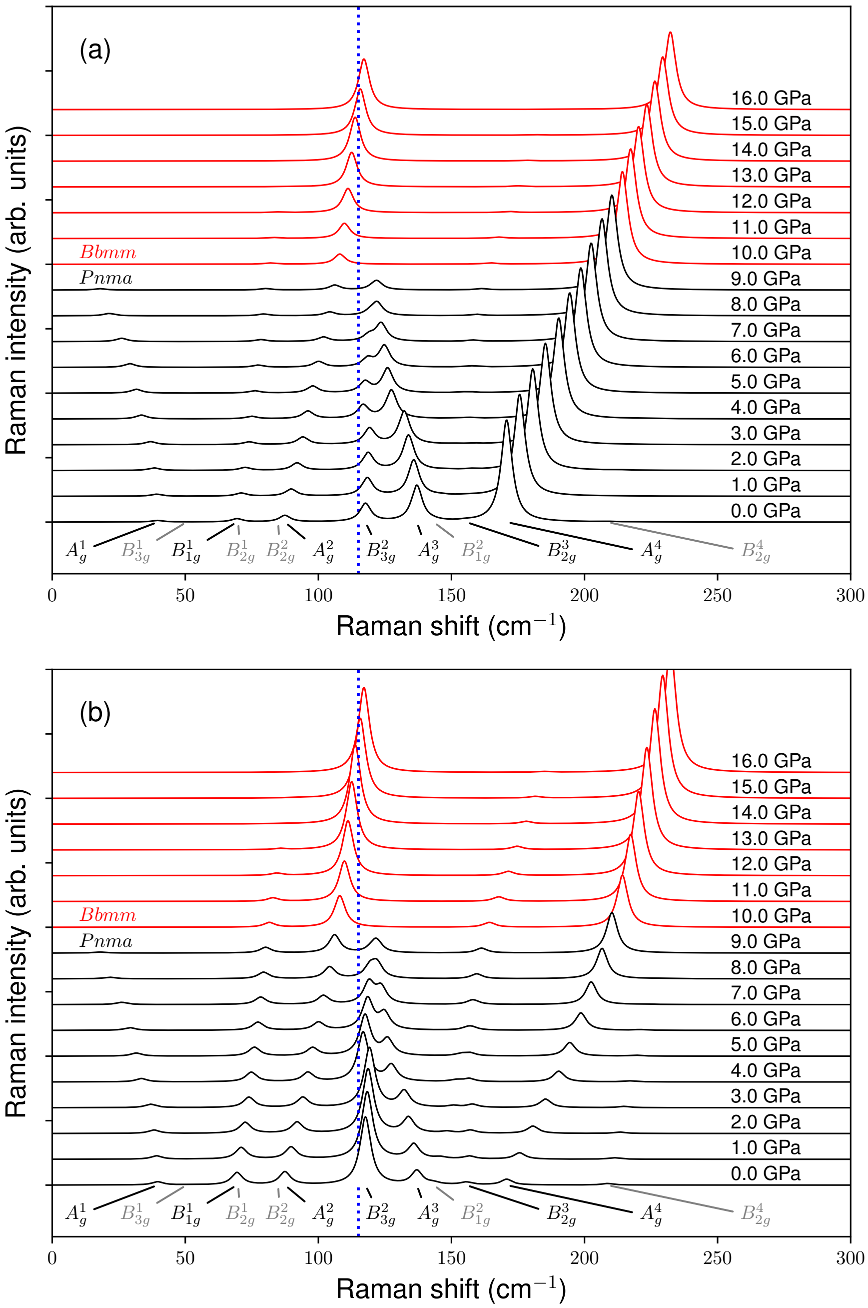

FIG. 6: Calculated pressure dependence of the polycrystalline (i.e. averaged Raman intensities over all possible crystal orientations) Raman spectra of SnSe with the incident electric field (a) parallel and (b) perpendicular to the sample. The black and red spectra correspond to the starting *Pnma* and the high-pressure *Bbmm* modifications, respectively. The vertical blue dashed line stands for the cutoff limit of the Raman filter used in the respective experimental high-pressure Raman spectroscopic investigations (Fig. 6 in the main text).

E. Optical properties of SnSe under pressure

The calculated FIR reflectance spectra of SnSe across the pressure-induced $Pnma \rightarrow Bbmm$ transition are displayed in Fig. 7. The spectra were derived from the dielectric function $\varepsilon(\omega)$, which was calculated from the dielectric constants, TO harmonic frequencies, oscillator strengths, and Lorentzian broadening parameters (see **Section I**). The energy loss function Im($-\frac{1}{\varepsilon(\omega)}$) was used for the evaluation of the respective LO mode frequencies for both the *Pnma*-SnSe and *Bbmm*-SnSe phases (Fig. 8).

TABLE VI: Results of the DFT-PBEsol0 Raman-active modes for the SnSe *Pnma* phase under external hydrostatic pressures. The respective mode assignments, mode frequencies ω_0, pressure dependence, and the isothermal γ_i^T mode Grüneisen parameters are provided. The latter have been calculated from the equation $\gamma_i^T = \frac{B_0}{\omega_0} \times \frac{\partial \omega}{\partial P}$, where we have used the calculated *Pnma* bulk modulus value $B_0 = 51.2$ GPa (Table II in the main text).

Mode assignment	ω_0 (cm^{-1})	$\frac{\partial \omega}{\partial P}$ (cm^{-1}/GPa)	$\frac{\partial^2 \omega}{\partial P^2}$ (cm^{-1}/GPa^2)	γ_i^T
A_g^1	39.6	-0.54	-0.21	-0.7
B_{3g}^1	50.47	2.07	-0.05	2.1
B_{1g}^1	69.4	1.5	-0.04	1.11
B_{2g}^1	69.9	-2.78	-0.13	-2.04
B_{2g}^2	84.9	3.38	-	2.04
A_g^2	87.42	2.05	-	1.2
B_{3g}^2	117.69	0.17	-	0.07
A_g^3	137.01	-2.79	-0.1	-1.04
B_{1g}^2	143.3	2.2	-0.03	0.79
B_{2g}^3	155.54	0.45	-	0.15
A_g^4	170.74	4.4	-	1.32
B_{2g}^4	208.57	1.95	-	0.48

TABLE VII: Results of the DFT-PBEsol0 Raman-active modes for the SnSe *Bbmm* phase under external hydrostatic pressures. The respective mode assignments, mode frequencies ω_0, pressure dependence, and the isothermal γ_i^T mode Grüneisen parameters are provided. The latter have been calculated from the equation $\gamma_i^T = \frac{B_0}{\omega_0} \times \frac{\partial \omega}{\partial P}$, where we have used the calculated *Bbmm* bulk modulus value $B = 95.2$ GPa (Table II in the main text).

Mode assignment	ω_0 (cm^{-1})	$\frac{\partial \omega}{\partial P}$ (cm^{-1}/GPa)	$\frac{\partial^2 \omega}{\partial P^2}$ (cm^{-1}/GPa^2)	γ_i^T
B_{2g}^1	66.03	2.49	-0.03	3.59
B_{1g}^1	81.28	2.29	-0.04	2.68
A_g^1	107.98	2	-0.02	1.76
B_{2g}^2	122.12	4.72	-0.04	3.68
B_{1g}^2	164.07	4.65	-0.05	2.7
A_g^2	214.1	3.61	-0.02	1.61

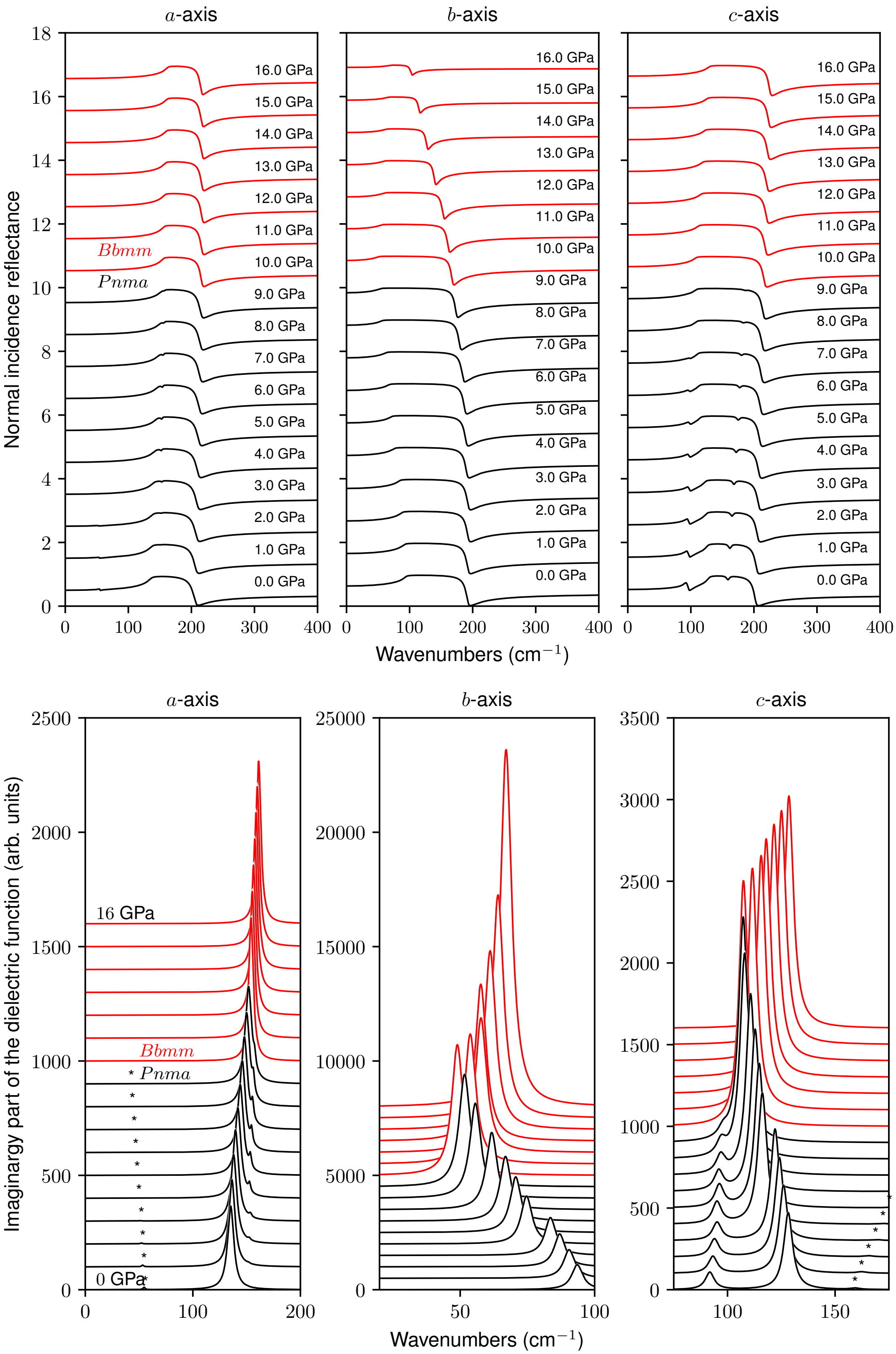

FIG. 7: Calculated DFT-PBEsol0 SnSe FIR reflectance spectra (top row) and imaginary part of the dielectric function (bottom row) of SnSe optimized under external hydrostatic pressures for the space groups *Pnma* and *Bbmm* for the three different crystallographic orientations.

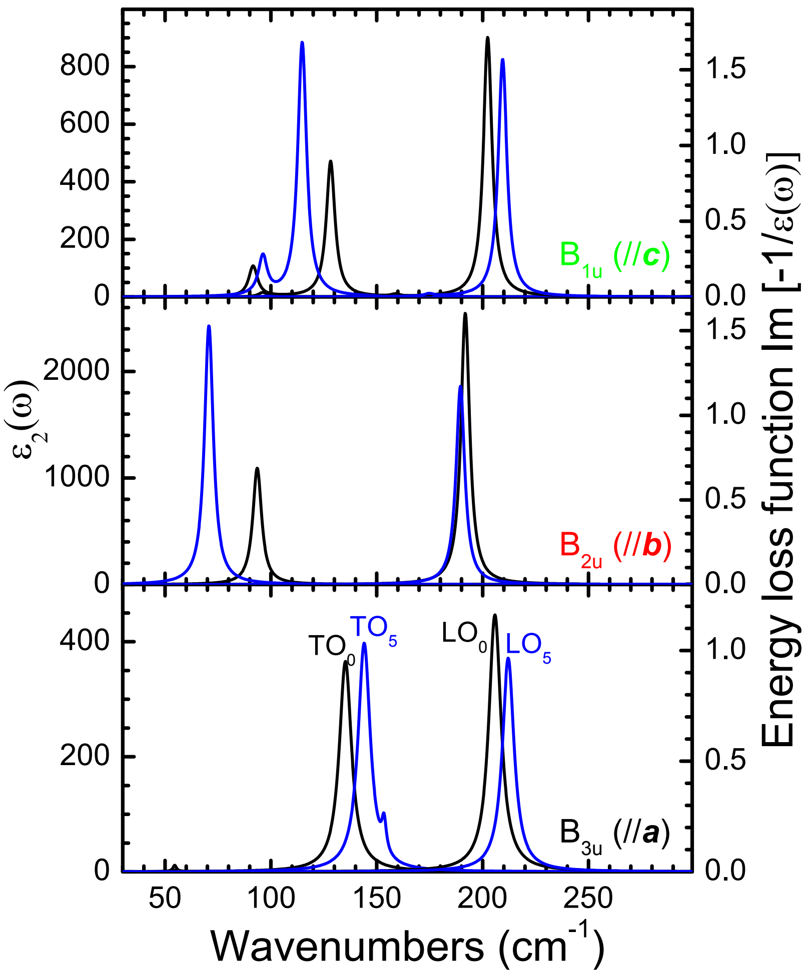

FIG. 8: Representative spectra of the imaginary part of the dielectric function $\varepsilon_2(\omega)$, and the energy loss function Im(-$\frac{1}{\varepsilon(\omega)}$) for the SnSe *Pnma* phase at 0 GPa (TO$_0$-LO$_0$, black, Table I) and at 5 GPa (TO$_5$-LO$_5$, blue) for the three different crystallographic axes, as calculated from the respective reflectance spectra (Fig. 7). The $\varepsilon_2(\omega)$ spectra show the TO modes, the Im(-$\frac{1}{\varepsilon(\omega)}$) spectra indicate the LO modes, and the corresponding LO-TO frequency splitting is plotted in Fig. 9 in the main text.

[1] E. I. Kamitsos, "Modern glass characterization," (John Wiley & Sons, Inc., 2015) Chap. 2, pp. 32–73.
[2] H. R. Chandrasekhar, R. G. Humphreys, U. Zwick, and M. Cardona, Phys. Rev. B **15**, 2177 (1977).
[3] C. Julien, M. Eddrief, I. Samaras, and M. Balkanski, Mater. Sci. Eng. B **15**, 70 (1992).
[4] T. Chattopadhyay, J. Pannetier, and H. G. von Schnering, J. Phys. Chem. Sol. **47**, 879 (1986).
[5] I. Loa, S. R. Popuri, A. D. Fortes, and J. W. G. Bos, Phys. Rev. Materials **2**, 085405 (2018).
[6] H. G. von Schnering and H. Wiedemeier, Z. Kristallogr. **156**, 143 (1981).
[7] M. Sist, J. Zhang, and B. B. Iversen, Acta Cryst. B **72**, 310 (2016).
[8] R. Dovesi, V. R. Saunders, C. Roetti, R. Orlando, C. M. Zicovich-Wilson, F. Pascale, B. Civalleri, K. Doll, N. M. Harrison, I. J. Bush, P. D'Arco, M. Llunell, M. Causà, and Y. Noël, "CRYSTAL14 User's Manual," University of Torino: Torino, 2014.
[9] M. Towler and C. Zicovich-Wilson, "Selenium basis sets for the crystal program," (1995).
[10] G. Sophia, *Ab-initio study of the dielectric response of high-permittivity perovskites for energy storage*, Ph.D. thesis, Univesité de Pau et des Pays de l'Adour and Università degli Studi di Torino, Turin (2014).
[11] B. Metz, H. Stoll, and M. Dolg, J. Chem. Phys. **113**, 2563 (2000).
[12] I. Loa, R. J. Husband, R. A. Downie, S. R. Popuri, and J.-W. G. Bos, J. Phys. Cond. Matt. **27**, 072202 (2015).
[13] X. Xu, Q. Song, H. Wang, P. Li, K. Zhang, Y. Wang, K. Yuan, Z. Yang, Y. Ye, and L. Dai, ACS Appl. Mater. Interfaces **9**, 12601 (2017).
[14] A. Kokalj, Comp. Mater. Sci. **28**, 155 (2003).
[15] G. J. Keeler and D. N. Batchelder, J. Phys. C: Solid State Phys. **5**, 3264 (1972).
[16] K. Syassen, High Press. Res. **28**, 75 (2008).
[17] S. Klotz, J.-C. Chervin, P. Munsch, and G. L. Marchand, J. Phys. D: Appl. Phys. **42**, 075413 (2009).
[18] I. Efthimiopoulos, M. Germer, S. Jahn, M. Harms, H. J. Reichmann, S. Speziale, U. Schade, M. Sieber, and M. Koch-Müller, High Press. Res. (2018), 10.1080/08957959.2018.1558223.